Speckle-learned convolutional neural network for the recognition of intensity degenerate orbital angular momentum modes

Venugopal Raskatla,*,† **Purnesh Singh Badavath**, **and Vijay Kumar***
National Institute of Technology Warangal, Department of Physics, Hanamkonda, Telangana, India

Abstract. Intensity degenerate orbital angular momentum (OAM) modes are impossible to recognize by direct visual inspection even using available machine learning techniques. We are reporting speckle-learned convolutional neural network (CNN) for the recognition of intensity degenerate Laguerre–Gaussian ($LG_{p,l}$) modes, intensity degenerate LG superposition modes, and intensity degenerate perfect optical vortices. The CNN is trained on the simulated one-dimensional far-field intensity speckle patterns of the corresponding intensity degenerate OAM modes. The trained CNN recognizes intensity degenerate OAM modes with an accuracy >99%. Speckle-learned CNNs are also capable of recognizing intensity degenerate OAM modes even under the presence of high Gaussian white noise and atmospheric turbulence with an accuracy >97%. © *2023 Society of Photo-Optical Instrumentation Engineers (SPIE)* [DOI: 10.1117/1.OE.62.3.036104]

Keywords: orbital angular momentum beams; perfect optical vortices; speckle; deep learning; convolutional neural network.

Paper 20220773G received Jul. 13, 2022; accepted for publication Feb. 14, 2023; published online Mar. 8, 2023.

1 Introduction

In today's world, artificial intelligence (AI) became an integral part of our life, and it is becoming a very versatile tool for researchers to come up with better and more accurate results. Machine learning and deep learning techniques are part of AI and augmenting complex physical systems for better understanding, physics, and optics are no exception. For the past two decades, the $LG_{p,l}$ beams[1] carrying orbital angular momentum (OAM) of $l\hbar$ per photon (where l is the topological charge and $\hbar$ is the reduced Planck's constant) have gained prominence because of its OAM degree of freedom. These beams are extensively used in the fields of optical trapping,[2] optical communication,[3–5] quantum entanglement, and quantum communication.[6] These OAM beams reveal a subtle connection between macroscopic and microscopic optics, it became very important to study and develop simple and feasible methods for the generation and detection of OAM modes. Traditional methods like interference, diffraction, and other[7–13] are cumbersome and require a precise alignment for high recognition accuracy. Although it is easy to identify distinct patterns by eye, the automation of the process for rapid detection is difficult. To overcome this problem machine learning and deep learning methods are been proposed and demonstrated for rapid detection of OAM modes with better accuracy.[14–21] Despite better accuracy, these are alignment limited and one needs to capture the entire mode. These limitations were overcome in the recent demonstration on the speckle-based CNN[22–24] and wavelet scattering network.[25]

The $LG_{p,l}$ modes (with $p = 0$) are the special subset of OAM beams described by radial index p and azimuthal index l (also called a charge). The $LG_{p,l}$ beams of the order p and $\pm l$ have identical intensity distributions therefore they cannot be distinguished by their sole

*Address all correspondence to Vijay Kumar, vijay@nitw.ac.in; Venugopal Raskatla, venuraskatla@gmail.com

†Current affiliation: Optoelectronics Research Centre and Centre for Photonic Metamaterials, University of Southampton, Highfield, Southampton, SO17 1BJ, United Kingdom

0091-3286/2023/$28.00 © 2023 SPIE

intensity images or their respective two-dimensional (2D) far-field speckle patterns[22–25] as well. A lot of work has been developed to measure and quantify the charge of these modes. The $\mathrm{LG}_{p,l}$ beams, also known as optical vortices are the center of attraction for many researchers but many times their use is limited because of their charge-dependent modal size. Using POVs, it becomes possible to generate optical vortices of any charge with the same modal size.[26] All the POVs visually look identical because of their identical intensity pattern and hence, these are also intensity degenerate OAM modes. The interference and diffraction-based methods are conventionally used to distinguish OAM degenerate modes from the orientation of their respective astigmatic transformed far-field patterns. The astigmatic transformation or the use of a cylindrical lens helps to develop a machine learning model[27–29] for their classification.

In this paper, we demonstrate speckle-learned CNN for the recognition of intensity degenerate, (i) OAM modes, (ii) OAM superposition modes, and (iii) POVs. We have trained a CNN on simulated one-dimensional (1D) far-field intensity speckle images of the respective intensity degenerate OAM modes. The 1D far-field can be experimentally realized using a cylindrical lens. To show the robustness of our model for experimental realization, we train and evaluate the network on the speckle patterns having very high Gaussian white noise (GWN) and on speckle patterns generated by modes distorted due to atmospheric turbulence effect.

2 Intensity Degenerate OAM Modes

2.1 *Laguerre–Gaussian ($\mathrm{LG}_{p,l}$) Modes*

The family of Laguerre–Gaussian ($\mathrm{LG}_{p,l}$) modes carrying OAM are the solutions of free space paraxial wave equation in a cylindrical coordinate system. Mathematically these $\mathrm{LG}_{p,l}$ modes are expressed as

$$\mathrm{LG}_{p,l}(\rho,\phi,z) = A_0\left(\frac{w_0}{w(z)}\right)\left(\frac{\rho}{w(z)}\right)^{|l|} L_p^{|l|}\left(\frac{2\rho^2}{w^2(z)}\right) \times \exp\left(-\frac{\rho^2}{w(z)^2}\right)\exp\left[-i\left(kz + k\frac{\rho^2}{2R(z)}\right)\right] \times \exp(il\phi)\exp[i(|l| + 2p + 1)\Phi(z)], \tag{1}$$

where A_0 is the amplitude, $R(z)$ is the wavefront curvature of the beam, $w(z)$ is the effective width of the beam, w_0 is the beam waist at $z = 0$, $\Phi(z)$ is the Gouy phase shift, p is a non-negative integer, l is an integer and $L_p^{|l|}$ is an associated Laguerre function of order p and l. For a given value of p, Eq. (1) gives the identical intensity profiles for modes $\mathrm{LG}_{p,l}$ and $\mathrm{LG}_{p,-l}$ since they are mutual conjugate modes. Using Eq. (1), we have considered eight such pairs of intensity degenerate $\mathrm{LG}_{p,l}$ modes with $p = 0$ and $l = \pm 1$ to ± 8.

2.2 *Superposition Modes*

The superposition of any $\mathrm{LG}_{p,l}$ modes with $p = 0$ are expressed as

$$\mathrm{SM}_{\{l\}}(\boldsymbol{r}) = \sum_l c_l \mathrm{LG}_{0,l}(\boldsymbol{r}), \tag{2}$$

where subscript $\{l\}$ denotes all the contributing $\mathrm{LG}_{0,l}$ modes and c_l is their corresponding weight. The modes $\mathrm{SM}_{\{l\}}$ and $\mathrm{SM}_{\{-l\}}$ are intensity degenerate mutual conjugate modes. We have considered eight pairs of intensity degenerate superposition modes: [$\mathrm{SM}_{\{1,-3\}}$, $\mathrm{SM}_{\{-1,3\}}$, $\mathrm{SM}_{\{2,6\}}$, $\mathrm{SM}_{\{-2,-6\}}$, $\mathrm{SM}_{\{3,-5\}}$, $\mathrm{SM}_{\{-3,-5\}}$, $\mathrm{SM}_{\{3,-7\}}$, $\mathrm{SM}_{\{-3,7\}}$, $\mathrm{SM}_{\{1,5,7\}}$, $\mathrm{SM}_{\{-1,-5,-7\}}$, $\mathrm{SM}_{\{2,8,-4\}}$, $\mathrm{SM}_{\{-2,-8,4\}}$, $\mathrm{SM}_{\{1,4,-2,-5\}}$, $\mathrm{SM}_{\{-1,-4,2,5\}}$, $\mathrm{SM}_{\{1,6,-2,-7\}}$, $\mathrm{SM}_{\{-1,-6,2,7\}}$].

2.3 *Perfect Optical Vortices (POVs)*

The $\mathrm{LG}_{p,l}$ and $\mathrm{SM}_{\{l\}}$ modal size is dependent on its charges, whereas in POVs the modal size is charge independent. The complex field amplitude of POV with ring width $2w_r$ and radius r_r is represented as[30]

$$\mathrm{PV}_l(r,\phi) = i^{l-1}\frac{w_g}{w_r}\exp(il\phi)\exp\left(-\frac{r^2+r_r^2}{w_r^2}\right)I_l\left(\frac{2rr_r}{w_r^2}\right), \tag{3}$$

where I_l is the l'th order modified Bessel function of the first kind and w_g is the beam waist of the Gaussian beam. It can be seen that all PV_l are intensity degenerate modes. We have considered 16 intensity degenerate POVs with $l = \pm 1$ to ± 8.

2.4 *Generation of 1D Far-field Speckles*

The 1D speckle far-fields of the intensity degenerate OAM modes are calculated as

$$U_j^{\mathrm{sc}}(\boldsymbol{x},\boldsymbol{y}) = \mathcal{F}_{1\mathrm{D}}\{U(\boldsymbol{r})e^{i\phi_{R_j}(\boldsymbol{x},\boldsymbol{y})}\}, \tag{4}$$

where $U(\boldsymbol{r}) = \{\mathrm{LG}_{p,l}(\boldsymbol{r})\ \mathrm{or}\ \mathrm{SM}_{\{l\}}(\boldsymbol{r})\ \mathrm{or}\ \mathrm{PV}_l(\boldsymbol{r})\}$, $\mathcal{F}_{1\mathrm{D}}$ is 1D fast Fourier transform (FFT) in the y-direction. The random phases, ϕ_{R_j} have uniformly distributed phase values between 0 and 2π with the smallest unit of the randomness of 4×4 pixels (shown in Fig. 1). The 1D far-field intensity speckle images (I_j^{sc}) corresponding to the 1D speckle far-field U_j^{sc} are simulated using, the equation

$$I_j^{\mathrm{sc}}(\boldsymbol{x},\boldsymbol{y}) = U_j^{\mathrm{sc}*}(\boldsymbol{x},\boldsymbol{y}) \times U_j^{\mathrm{sc}}(\boldsymbol{x},\boldsymbol{y}). \tag{5}$$

Figures 2(a)–2(c) show the samples of the intensity, phase, and 1D far-field intensity speckle patterns of intensity degenerate $\mathrm{LG}_{p,l}$ $\mathrm{SM}_{\{l\}}$ and PV_l modes. Each pair of modes have an identical intensity profile and mutual conjugate phases. Since the Fourier transform is taken only along one dimension, the speckles are not evenly distributed in vertical and horizontal directions, and charge information of intensity degenerate modes is present in the distribution and orientation of the speckle patterns. This can be analogously visualized by taking 1D FFT of direct modes: $U_j(\boldsymbol{x},\boldsymbol{y}) = \mathcal{F}_{1\mathrm{D}}\{U(\boldsymbol{r})\}$ [Fig. 1(b)]. It can be easily seen that different amount of shear (dislocation in strips) is introduced in the beams carrying different OAM [It should be noted that we only used 1D FFT speckles of direct beams for training in this paper, not those shown in Fig. 1(b)]. For $\mathrm{LG}_{p,l}$ and $\mathrm{SM}_{\{l\}}$ modes, the speckle size in the vertical (y-) direction ranges from 14 to 22 pixels whereas in the horizontal (x) direction it ranges from 8 to 16 pixels. For PV_l modes the speckle size is ~24 pixels in the vertical direction and 8 pixels in the horizontal direction for all the modes.

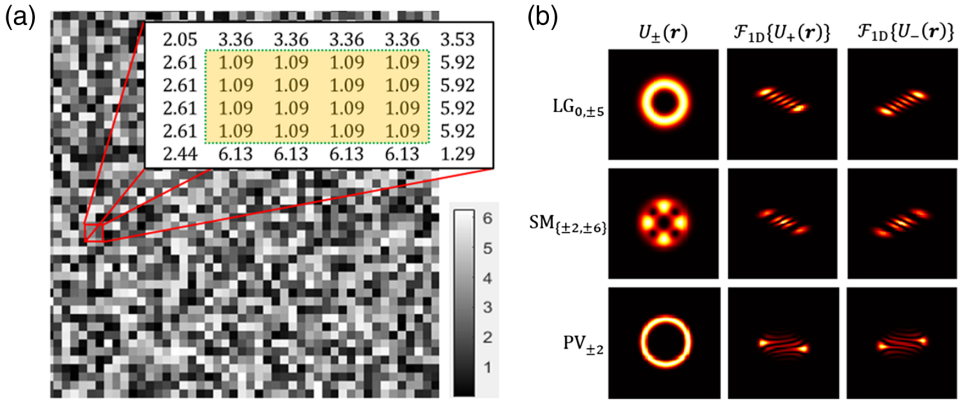

Fig. 1 (a) The random phase $\phi_{R_j}(x,y)$ with the smallest unit of the randomness of 4×4 pixels used to simulate the speckle patterns. (b) Intensity distribution of original OAM and their 1D FFT field.

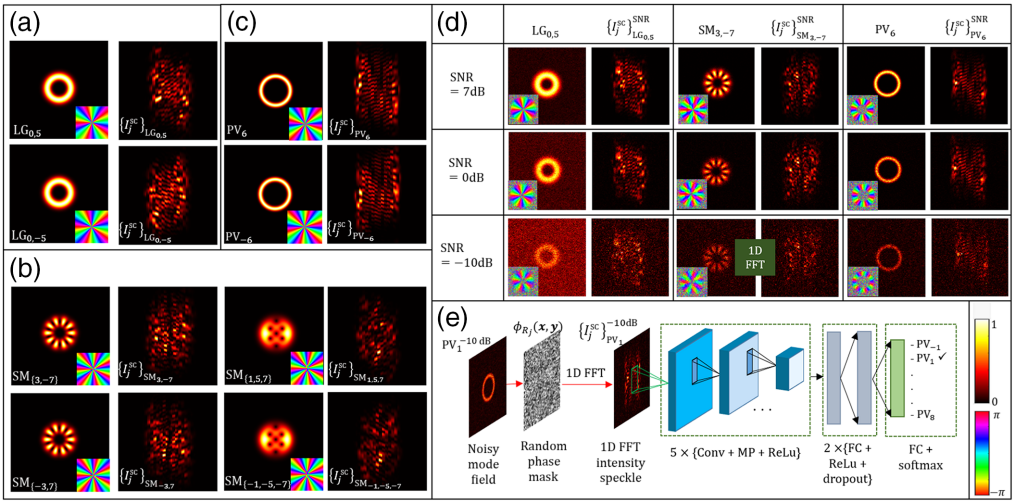

Fig. 2 The intensity and phase patterns of the intensity degenerate modes and their respective 1D far-field intensity speckle images of (a) $LG_{p,l}$, (b) $SM_{\{l\}}$, and (c) PV_l. (d) OAM modes and their respective speckle images in presence of GWN. For better visualization of the noise effect, the modes are passed through the same random phase mask so that speckle distribution remains the same and only the noise effect will vary. (e) Workflow for training CNN model for recognition of PV_l modes.

2.5 *Gaussian White Noise (GWN)*

To simulate realistic experimental scenarios and to make our model more robust, the GWN is added to the modes. The GWN is quantified by specifying SNR (in dB)

$$\mathrm{SNR}_{\mathrm{dB}} = 10\log_{10}\left(\frac{P_{\mathrm{signal}}}{P_{\mathrm{noise}}}\right). \tag{6}$$

Here, the power (P of signal and noise) is defined as

$$P = \frac{1}{N}\sum_{n=1}^{N} I(n). \tag{7}$$

Here, $I(n)$ is the intensity of n'th pixel in an image with total N pixels. We have generated data and trained the network for seven different noise levels ranging from 0.1 to 10 times the input signal power. The SNR values used for generating these seven datasets are 10, 7, 3, 0, −3, −7, and −10 dB. Figure 2(d) shows the intensity distributions of the modes with additive noise and the corresponding 1D far-field intensity speckle images.

2.6 *Atmospheric Turbulence*

For simulating atmospheric turbulence, we have generated a turbulence phase screen using a modified atmospheric spectrum model.[31] For this model, the refractive index power spectral density is given as

$$\Phi_n(\kappa) = 0.033C_n^2\left[1 + 1.802\left(\frac{\kappa}{\kappa_l}\right) - 0.254\left(\frac{\kappa}{\kappa_l}\right)^{\frac{7}{6}}\right]\exp\left(-\frac{\kappa^2}{\kappa_l^2}\right)(\kappa^2 + \kappa_0^2)^{-\frac{11}{6}}, \tag{8}$$

where C_n^2 is the refractive index structure parameter determining the turbulence strength, $k_l = 3.3/l_0$, $k_0 = 2\pi/L_0$, l_0 and L_0 are the internal and external scales, respectively. The phase screen is synthesized by multiplying $\Phi_n(\kappa)$ by a complex random matrix, C_R, with mean 0 and variance 1, and then taking its Fourier transform. Here, Fourier transforms produced two

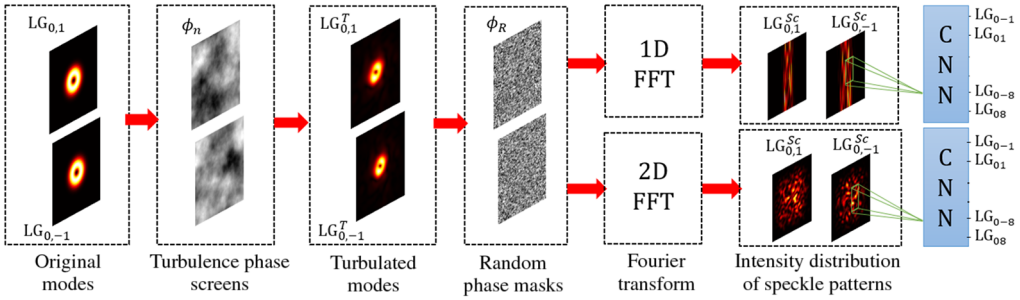

Fig. 3 The atmospheric turbulence effect is realized by passing $LG_{p,l}$ modes through turbulence phase screen generated with $C_n^2 = 1 \times 10^{-14}$ $m^{-2/3}$. The resultant turbulated modes are then passed through a random phase mask to generate a corresponding speckle field and the intensity images of speckle patterns at a Fourier plane generated by taking 1D/2D FFT are fed to CNN to build a classification model.

uncorrelated real and imaginary parts of the phase screen. We have taken only the real part and discarded the imaginary part

$$\phi_n = \text{real}(\mathcal{F}_{2D}\{C_R \times \Phi_n(\kappa)\}). \tag{9}$$

For generating turbulated modes, the $LG_{p,l}$ and $SM_{\{l\}}$ are first multiplied with an atmospheric turbulence phase screen synthesized by taking $C_n^2 = 1 \times 10^{-14}$ $m^{-2/3}$, $l_0 = 0.001$ m and $L_0 = 100$ m. These turbulated modes are multiplied with a random phase mask to generate the speckle fields and then intensity images are saved to generate the corresponding dataset as shown in Fig. 3.

3 Speckle-learned Convolutional Neural Network

For each mode, $LG_{p,l}$, $SM_{\{l\}}$, and PV_l, we have simulated eight datasets $\{I_j^{sc}\}^{SNR}_{LG\text{ or }SM\text{ or }PV}$ of 1D far-field intensity speckle images corresponding to seven SNR levels and one without any GWN. We have also simulated one dataset for $LG_{p,l}$ and $SM_{\{l\}}$ modes having distortion due to atmospheric turbulence. Datasets $\{I^{sc}_{j=1-1000}\}^{SNR}_{LG\text{ or }SM}$ belonging to $LG_{p,l}$ and $SM_{\{l\}}$ modes have 1000 images per class [16 $LG_{p,l}$ classes with $l = \pm 1$ to ± 8 and 16 $SM_{\{l\}}$ classes defined after Eq. (2)] and datasets $\{I^{sc}_{j=1-2000}\}^{SNR}_{PV}$ belonging to PV_l modes have 2000 images per class (16 PV_l classes with $l = \pm 1$ to ± 8). In all the datasets, each speckle image is of size $256 \times 256 \times 3$ pixels and generated by taking the random phase ($\phi_{R_j}(\boldsymbol{x}, \boldsymbol{y})$).

These datasets are fed to CNN to build a classification model. We have used Alexnet,[32] a pretrained CNN known for its moderate computational load and high accuracy. Alexnet has a very simple architecture and it is trained for more than a million images to classify 1000 categories. It has five convolutional layers and three fully connected layers. Convolutional layers perform convolution operations on input images using filters. Different filters are used to extract different features as an image is passed through various convolutional layers. A large number of convolved features are extracted during the convolution operation and hence, the pooling layers are used to reduce computational load to process the data and to extract dominant features that are positional and rotational invariant. In the Alexnet, max pooling layers have been used that return the maximum value of the portion covered by the kernel.

For faster training, a rectified linear unit (ReLU) is used as a non-linear activation function that activates neurons by maintaining the positive values and clamping negative values to zero. After this, a dropout layer is added with a dropout rate of 50%. This means each neuron is turned off with a probability of 0.5 during each iteration and does not contribute to learning in that iteration. This leads a neuron to learn more robust features as each iteration has used different samples of the model's parameters. The use of dropout layers avoids the overfitting of the model. Two fully connected layers with ReLU activation and dropout layers are used to combine all the

Table 1 Comparison of classification accuracies of the networks trained on 1D and 2D far-field speckle images.

Modes		$\{I_j^{sc}\}_{LG}^{SNR}$		$\{I_j^{sc}\}_{SM}^{SNR}$		$\{I_j^{sc}\}_{PV}^{SNR}$	
FFT		1D FFT (%)	2D FFT (%)	1D FFT (%)	2D FFT (%)	1D FFT (%)	2D FFT (%)
Without any noise (dB)		>99	>50	>99	>50	>99	>40
With GWN	SNR = 10	>99	>49	>99	>50	>98	>39
	SNR = 7	>99	>49	>99	>49	>98	>37
	SNR = 3	>99	>49	>99	>48	>98	>35
	SNR = 0	>99	>48	>98	>45	>97	>31
	SNR = −3	>99	>46	>98	>40	>94	>26
	SNR = −7	>99	>38	>97	>37	>78	>19
	SNR = −10	>99	>33	>94	>27	>62	>12
Atmospheric turbulence, $C_n^2 = 1 \times 10^{-14}$ m$^{-2/3}$		>97	50	>97	>49	—	—

features extracted by convolutional layers. The softmax function is used as an activation function for the final fully connected layer to give the relative probability of each class.

We have modified this last layer to classify 16 modes retaining the weights and biases learned by the network. These weights and biases are updated during the training of our networks. The size of the input layer of Alexnet is $227 \times 227 \times 3$ pixels, hence it accepts images of this size only. We have processed our datasets and resized all images to $227 \times 227 \times 3$ pixels before feeding them to the network. The network is separately trained and tested for each dataset. Figure 2(e) shows the modified Alexnet network trained for the identification of POVs and a similar network is used for the identification of $LG_{p,l}$ and $SM_{\{l\}}$ modes. For each model, 80% of the images of the dataset are used for training and the remaining images are used for evaluation purposes. We have used the "stochastic gradient descent with momentum" (SGDM) algorithm with a constant learning rate of 0.0001 and momentum of 0.9. All processing, training, and evaluation are done on a single i7 9700 CPU with 32 GB RAM in MATLAB 2021b.

4 Results and Analysis

Table 1 shows the classification accuracy obtained for each dataset. The results show that the network classifies all the non-noisy modes with an accuracy of >99% indicating that it can very well distinguish the intensity degenerate modes. As the noise level increases (decreasing SNR values), the classification accuracy of the network for $LG_{p,l}$ modes are unaffected whereas it decreases for $SM_{\{l\}}$, and PV_l modes. In a case, when the noise level is 10 times the input (SNR = −10 dB), the accuracy drops to 94% for $SM_{\{l\}}$ and 62% for PV_l modes. It also shows that the network can recognize turbulated intensity degenerate $LG_{p,l}$ and $SM_{\{l\}}$ with an accuracy >97%.

5 Comparison with Network Trained on 2D Far-field Speckle Images

For comparison with the network trained on 2D far-field speckle images,[24] wherein the CNN was trained on intensity speckle images $I_j^{sc}(\boldsymbol{x},\boldsymbol{y})$ [Eq. (5)], where, $U_j^{sc}(\boldsymbol{x},\boldsymbol{y}) = \mathcal{F}_{2D}\{U(\boldsymbol{r})e^{i\phi_{R_j}(\boldsymbol{x},\boldsymbol{y})}\}$. All the hyperparameters are kept same, for generating 2D far-field speckles and for training the networks. Figure 4 shows the 1D and 2D far-field speckle intensity distribution of $LG_{p,l}$, $SM_{\{l\}}$ and PV_l modes. From Fig. 4, it can be easily seen that the speckle distribution in 2D far-field

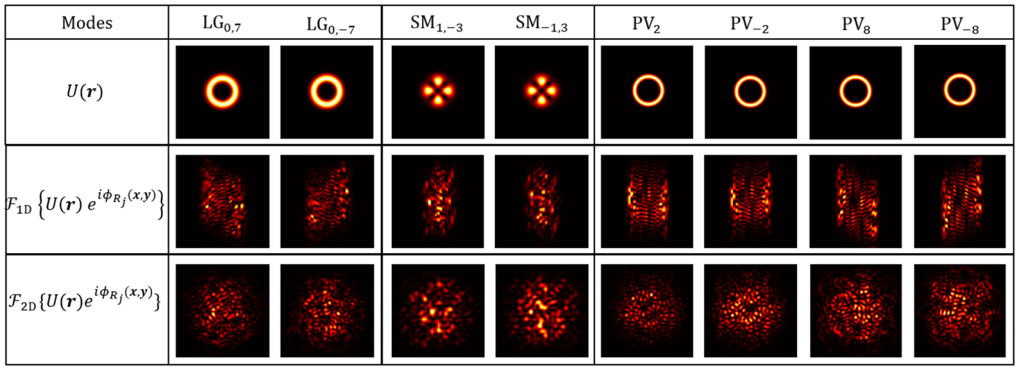

Fig. 4 1D and 2D far-field intensity speckle patterns of OAM modes. The same random phase mask is used for generating speckle fields of a given pair of degenerate modes. For better visualization, the speckle pattern corresponding to the degenerate mode pair is generated using the same random phase $\phi_{R_j}(x, y)$. The shown speckle patterns are without any GWN.

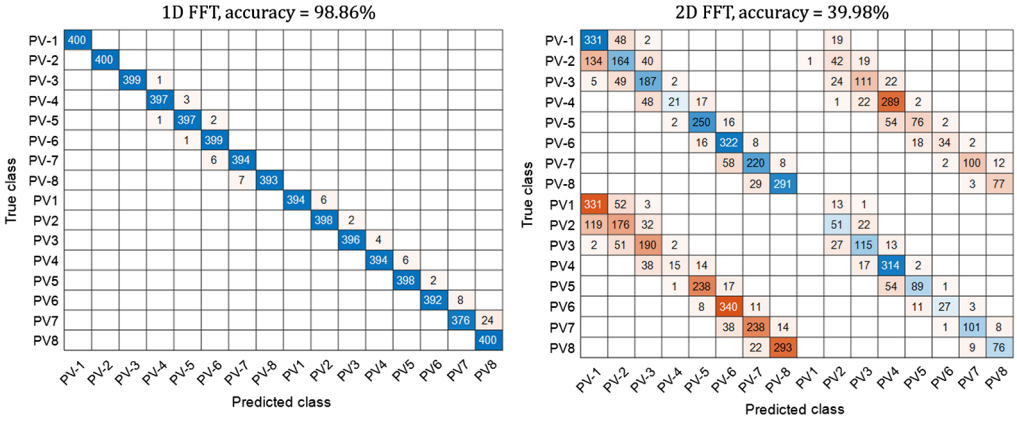

Fig. 5 Confusion matrices for PV_l modes with SNR $= 10$ dB. The confusion matrix to the left side corresponds to the model trained using 1D far-field intensity speckle images and that on the right side corresponds to the model trained using 2D far-field intensity speckle images.

speckle intensity images is the same for the degenerate mode whereas it is different in 1D far-field speckle intensity images. The comparative results of the network trained using 1D and 2D far-field intensity speckle images are also shown in Table 1. Figure 5 shows the confusion matrices of networks trained for 1D and 2D speckle images. From Table 1 and Fig. 4, it can be seen that the network trained for 2D far-field speckle intensity images confuses degenerate modes whereas the network trained on 1D far-field speckle intensity images accurately recognizes them.

For $LG_{p,l}$ and $SM_{\{l\}}$ the speckle size varies with the modes and they remain the same for all PV_l modes. As the network has learned to recognize all three types of modes, we can conclude that speckle size is certainly not the feature the model is looking for and the network has learned the underlying features of speckle distribution to accurately recognize modes. The physical understanding of the features learned by the network is an open research problem. Intuitively, the features hidden in the 2D far-field intensity speckle patterns of degenerate modes have some kind of spatial symmetry and hence, the network fails to recognize them. To break the symmetry, we have taken 1D FFT in place of 2D FFT to perform the astigmatic transformation.

6 Summary and Conclusion

We demonstrated a speckle-learned CNN for the recognition of intensity degenerate OAM modes. The network is trained and evaluated on the 1D far-field intensity speckle images

corresponding to intensity degenerate OAM modes ($LG_{p,l}$, $SM_{\{l\}}$, and PV_l without GWN) separately and achieved an accuracy of >99%. The 1D far-field intensity speckle images of the respective OAM modes can be easily realized in experiments using a cylindrical lens. The main idea behind this technique is to break the symmetry in speckle distribution of intensity degenerate modes by astigmatic transformation. For robustness and general experimental scenario, we have also trained and tested the network for seven different noise levels and showed that network works well even when the noise level is the same as that of the input signal (SNR = 0 dB). Thus we believe that our method is powerful enough to recognize degenerate OAM modes or any modes in general, even in the presence of large noise. This method is also robust against the atmospheric turbulence effects as well. The network can be made more and more robust by training it on the speckle patterns of the respective OAM modes using the random phase masks with the different units of randomness.[24] The proposed speckle-learned technique also lifts the alignment constraint for modal recognition. It is already established that any region of the speckle field containing sufficient speckle grains can be used for modal recognition,[24,25] and we strongly believe that the same holds for 1D speckle fields. However, a comprehensive study on modal recognition using different regions of the speckle field is outside the scope of the current paper and will be presented in future work along with additional results.

It is important to note that the method presented in this paper is different than those used for noise removal.[33,34] Even though CNN-based speckle and Gaussian noise removal methods use similar deep neural layers and activation functions, the presented speckle-based CNN method learns differently. Here instead of removing noise, the CNN layers look for underlying OAM features, and noises are automatically eliminated in the process as they do not possess any specific pattern, and hence do not contribute to the key features of the OAM field. Compared to these noise removal networks, our CNN network is much simpler and easy to train without any loss of generality.

Acknowledgments

VK acknowledges the SERB grant (SRG/2021/001375) and NITW RSM grant (Head Code: P1138). The authors declare no conflicts of interest.

Data Availability

Data underlying the results presented in this paper are available upon reasonable request from the authors.

References

1. L. Allen et al., "Orbital angular momentum of light and the transformation of Laguerre-Gaussian laser modes," *Phys. Rev. A* **45**(11), 8185–8189 (1992).
2. D. G. Grier, "A revolution in optical manipulation," *Nature* **424**(6950), 810–816 (2003).
3. G. Gibson et al., "Free-space information transfer using light beams carrying orbital angular momentum," *Opt. Express* **12**(22), 5448 (2004).
4. A. Trichili et al., "Optical communication beyond orbital angular momentum," *Sci. Rep.* **6**(1), 27674 (2016).
5. A. E. Willner et al., "Orbital angular momentum of light for communications," *Appl. Phys. Rev.* **8**(4), 041312 (2021).
6. M. Erhard et al., "Twisted photons: new quantum perspectives in high dimensions," *Light Sci. Appl.* **7**(3), 17146–17146 (2018).
7. M. Harris et al., "Laser modes with helical wave fronts," *Phys. Rev. A* **49**(4), 3119–3122 (1994).
8. H. I. Sztul and R. R. Alfano, "Double-slit interference with Laguerre-Gaussian beams," *Opt. Lett.* **31**(7), 999 (2006).
9. C.-S. Guo, L.-L. Lu, and H.-T. Wang, "Characterizing topological charge of optical vortices by using an annular aperture," *Opt. Lett.* **34**(23), 3686 (2009).

10. L. E. E. de Araujo and M. E. Anderson, "Measuring vortex charge with a triangular aperture," *Opt. Lett.* **36**(6), 787–789 (2011).
11. M. N. Jacobs et al., "High-resolution, wavefront-sensing, full-field polarimetry of arbitrary beams using phase retrieval," *Opt. Express* **30**(15), 27967 (2022).
12. Y. Esashi et al., "Ptychographic amplitude and phase reconstruction of bichromatic vortex beams," *Opt. Express* **26**(26), 34007 (2018).
13. L. Rego et al., "Generation of extreme-ultraviolet beams with time-varying orbital angular momentum," *Science* **364**(6447), eaaw9486 (2019).
14. M. Krenn et al., "Communication with spatially modulated light through turbulent air across Vienna," *New J. Phys.* **16**(11), 113028 (2014).
15. M. Krenn et al., "Twisted light transmission over 143 km," *Proc. Natl. Acad. Sci.* **113**(48), 13648–13653 (2016).
16. T. Doster and A. T. Watnik, "Machine learning approach to OAM beam demultiplexing via convolutional neural networks," *Appl. Opt.* **56**(12), 3386 (2017).
17. S. Lohani et al., "On the use of deep neural networks in optical communications," *Appl. Opt.* **57**(15), 4180 (2018).
18. A. Bekerman et al., "Beam profiler network (BPNet): a deep learning approach to mode demultiplexing of Laguerre–Gaussian optical beams," *Opt. Lett.* **44**(15), 3629 (2019).
19. L. R. Hofer et al., "Hermite–Gaussian mode detection via convolution neural networks," *J. Opt. Soc. Am. A* **36**(6), 936 (2019).
20. S. Sharifi et al., "Towards classification of experimental Laguerre–Gaussian modes using convolutional neural networks," *Opt. Eng.* **59**(7), 076113 (2020).
21. X. Fu, Y. Bai, and Y. Yang, "Measuring OAM by the hybrid scheme of interference and convolutional neural network," *Opt. Eng.* **60**(6), 064109 (2021).
22. V. Raskatla and V. Kumar, "Deep learning assisted OAM modes demultiplexing," *Proc. SPIE* **12126**, 121260A (2021).
23. V. Raskatla and V. Kumar, "Deep learning assisted classification of noisy Laguerre Gaussian modes," in *Front. in Opt. + Laser Sci.*, OSA, Washington, DC, p. JTu1A.16 (2021).
24. V. Raskatla et al., "Speckle-based deep learning approach for classification of orbital angular momentum modes," *J. Opt. Soc. Am. A* **39**(4), 759 (2022).
25. V. Raskatla, P. S. Badavath, and V. Kumar, "Convolutional networks for speckle-based orbital angular momentum modes classification," *Opt. Eng.* **61**(3), 036114 (2022).
26. A. S. Ostrovsky, C. Rickenstorff-Parrao, and V. Arrizón, "Generation of the 'perfect' optical vortex using a liquid-crystal spatial light modulator," *Opt. Lett.* **38**(4), 534 (2013).
27. P. Wang et al., "Convolutional neural network-assisted optical orbital angular momentum recognition and communication," *IEEE Access* **7**, 162025–162035 (2019).
28. B. P. da Silva et al., "Machine-learning recognition of light orbital-angular-momentum superpositions," *Phys. Rev. A* **103**(6), 063704 (2021).
29. V. Raskatla and V. Kumar, "Deep learning assisted recognition of perfect optical vortices through astigmatic transformed speckle patterns," in *Front. in Opt. + Laser Sci. (FIO, LS)*, Optica Publishing Group, Rochester, New York, p. JTu5A.23 (2022).
30. P. Vaity and L. Rusch, "Perfect vortex beam: Fourier transformation of a Bessel beam," *Opt. Lett.* **40**(4), 597 (2015).
31. L. C. Andrews and R. L. Phillips, *Laser Beam Propagation Through Random Media*, 2nd ed., SPIE Press, Bellingham, Washington (2005).
32. A. Krizhevsky, I. Sutskever, and G. E. Hinton, "ImageNet classification with deep convolutional neural networks," *Commun. ACM* **60**(6), 84–90 (2017).
33. P. Wang, H. Zhang, and V. M. Patel, "SAR image despeckling using a convolutional neural network," *IEEE Signal Process. Lett.* **24**(12), 1763–1767 (2017).
34. D. Li et al., "Speckle noise removal based on structural convolutional neural networks with feature fusion for medical image," *Signal Process. Image Commun.* **99**, 116500 (2021).

Venugopal Raskatla completed his 3-year master's degree, MSc (Tech) in engineering physics with photonics specialization at the National Institute of Technology, Warangal, India, in 2022. Currently, he is pursuing his PhD in the field of nanophotonics at the Nanophotonics & Metamaterials Group, Optoelectronics Research Centre, University of Southampton, UK.

His research interest includes unfolding the mysteries of the optics and photonics world with artificial intelligence.

Purnesh Singh Badavath received his integrated master's degree from the National Institute of Technology Agartala in 2020. Currently, he is pursuing a PhD under the guidance of Vijay Kumar in the Department of Physics, National Institute of Technology Warangal, India. His research work includes the application of artificial intelligence in optical communications using orbital angular momentum beams.

Vijay Kumar received his PhD from the University of Hyderabad in 2015. Currently, he is an assistant professor in the Department of Physics, National Institute of Technology Warangal, India. His research interest includes singular optics, nano-optics, light-matter interaction, optical communication, fiber optics, and machine learning.